



# Multiphase Simulation on the Collision, Transport, and Removal of Non-metallic Inclusions in the Molten Steel During RH Refining

KAIYU PENG, JUJIN WANG, QILAN LI, CHANG LIU, and LIFENG ZHANG

The initial size distribution of inclusions in the molten steel during the Ruhrstahl–Heraeus (RH) refining was investigated through an industrial trial. A three-dimensional numerical model for the steel-argon multiphase fluid flow and the collision, transport, and removal of inclusions in the steel was established to simulate the evolution of inclusions during the RH refining. The particle-size-grouping (PSG) method was applied to evaluate the collision of inclusions, which divided inclusions into sixteen groups with a volume ratio of 2.5 between adjacent groups. Detected inclusions were mostly  $\text{Al}_2\text{O}_3$  in aggregations or clusters. The initial number density of inclusions with diameter less than  $1\ \mu\text{m}$  was closed to  $1 \times 10^{15}\ \#/\text{m}^3$ , while that with diameter greater than  $10\ \mu\text{m}$  was less than  $1 \times 10^{10}\ \#/\text{m}^3$ . The calculated total oxygen content in the steel dropped from 251 to 93 ppm in approximately 10 minutes and was 14 ppm after refining for 1800 seconds which agreed well with measured ones. The removal fraction of inclusions increased with the refining time, while the removal rate showed a decrease. The removal fraction was larger than 90 pct at 1800 seconds, indicating a high efficiency of the RH refining in removing inclusions. After 300 seconds of collision, the number density of small inclusions with diameter less than  $2.5\ \mu\text{m}$  declined apparently from  $10^{13}$  to  $10^{15}\ \#/\text{m}^3$  to  $10^{12}\ \#/\text{m}^3$ . The distribution of inclusions and the total oxygen content in the steel was position-dependent. Due to the removal condition at the steel surface in the ladle, the number density of inclusions and the total oxygen in the steel near the steel surface and near the zone between two snorkels in the ladle had a minimum value, while that near the side wall of the ladle showed a relatively higher value. The gradient of the T.O content in the cross section near the free surface of the ladle was relatively large, around 15 ppm on the side and less than 2 ppm in the center.

<https://doi.org/10.1007/s11663-023-02736-1>

© The Minerals, Metals & Materials Society and ASM International 2023

## I. INTRODUCTION

A Ruhrstahl–Heraeus (RH) vacuum degasser is a second-refining furnace for removing the hydrogen, nitrogen, carbon, and inclusions in the molten steel, which is essential in manufacturing ultra-low-carbon steels.<sup>[1]</sup> A RH furnace consists of a ladle, an up-leg snorkel, a down-leg snorkel, and a vacuum chamber.

Argon gas is often poured into the up-leg snorkel through several nozzles to lift the molten steel and to promote the circulation, as shown in Figure 1. During this process, inclusions in the molten steel circulate in the steel and collide with each other.<sup>[2]</sup> Inclusions will be removed through the slag absorption once they move to the free surface of the top slag.<sup>[3]</sup>

For the production of ultra-low-carbon steels, aluminum is generally used to kill the oxygen in the molten steel, resulting in a large amount of aluminum oxide inclusions.<sup>[3,4]</sup> These generated alumina inclusions will collide and grow into large alumina clusters, which can cause defects in steels if some of the clusters remain in the steel product.<sup>[5,6]</sup> The RH furnace is a quite important and efficient process to remove these alumina clusters. The removal of inclusions in the steel is closely related to the flow field of the steel and the motion of inclusions. Many studies have focused on the flow field<sup>[7–11]</sup> and inclusions removal<sup>[12–17]</sup> during the RH refining process.

KAIYU PENG and QILAN LI are with the School of Metallurgical and Ecological Engineering, University of Science and Technology Beijing (USTB), Beijing 100083, P.R. China. JUJIN WANG and LIFENG ZHANG are with the School of Mechanical and Materials Engineering, North China University of Technology, Beijing 100144, P.R. China. Contact e-mails: wangjujin@ncut.edu.cn; zhanglifeng@ncut.edu.cn CHANG LIU is with the State Key Laboratory of Refractories and Metallurgy, Wuhan University of Science and Technology, Wuhan 430081, Hubei, P.R. China and also with the Key Laboratory for Ferrous Metallurgy and Resources Utilization of Ministry of Education, Wuhan University of Science and Technology, Wuhan 430081, Hubei, P.R. China.

Manuscript submitted November 21, 2022; accepted January 18, 2023.

Article published online February 21, 2023.

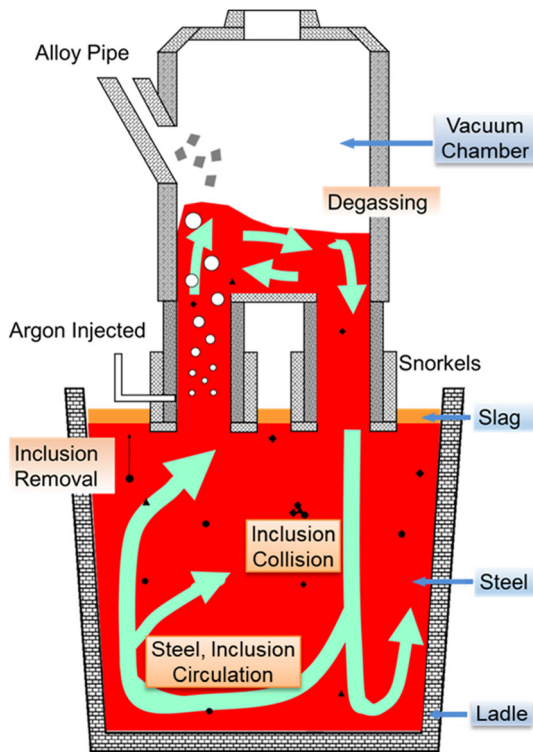


Fig. 1—Schematic of the fluid flow phenomena and the motion of inclusions in the molten steel of a RH refining furnace.

The fluid flow in the RH furnace has been studied extensively both through water models<sup>[7,11,18]</sup> and numerical models.<sup>[8,12,13,19,20]</sup> Discrete phase model (DPM) for the motion of argon bubbles was often used to simulate the flow field in the RH ladle. Turbulent characteristics of the fluid were accurately predicted by employing  $k-\epsilon$  two equations model. The motion and size evolution of inclusions in the molten steel were extremely complex, which involved the nucleation through deoxidation reactions, growth due to the collision and coalescence, adhesion by the refractory, and removal at the steel–slag interface.<sup>[21–25]</sup> As for the RH refining without aluminum addition, the collision and removal are two main factors affecting the distribution of the size and population of inclusions. It is generally known that the collision of inclusions in the molten steel contained three mechanisms: Brownian collision, Stokes collision, and turbulent collision, which are closely related to the fluid flow and turbulent features during the refining process. It was reported that the growth of inclusions with diameter smaller than  $1 \mu\text{m}$  was mainly controlled by the Brownian collision, while for inclusions with diameter larger than  $2 \mu\text{m}$ , the growth was mainly controlled by the turbulent collision and Stokes collision.<sup>[26]</sup> Population balance equations (PBEs) were usually used to model the size evolution of inclusions or bubbles<sup>[27–30]</sup> in the molten steel. Through coupling Computational Fluid Dynamic (CFD) and PBEs, the transport phenomena of inclusions in the molten steel can be simulated.<sup>[23,27,31]</sup> Chen *et al.*<sup>[17,32,33]</sup> simulated the distribution of inclusions in a single or double snorkel RH using the CFD-PBE model, where the turbulent collision, Stokes collision, the

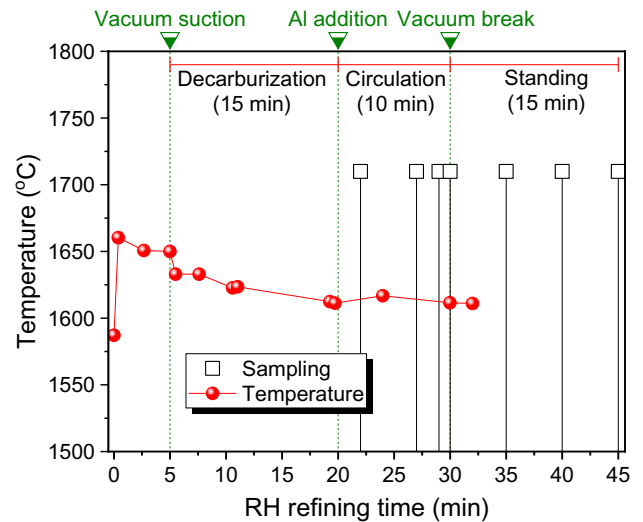


Fig. 2—Sampling and operation during the RH refining process.

inclusions removal at the steel–slag interface, and the inclusions removal by refractory adhesion were considered. Chen *et al.*<sup>[31]</sup> developed a three-dimensional CFD-PBE model to simulate the agglomeration, transport, and removal of  $\text{Al}_2\text{O}_3$  clusters. Shirabe *et al.*<sup>[12]</sup> studied the two-dimensional flow field of the molten steel and the collision and coalescence during the RH refining process. However, in these studies, an empirical exponential relation between the number density and the radius of inclusions was assumed<sup>[17,32,33]</sup> for the initial distribution of inclusions in the molten steel. Besides, only flow field of the molten steel was considered. In other words, single-phase models were used to simulate the flow in the RH degasser, ignoring the influence of interphase interaction between the steel, slag, and air phases.

In the current study, an industrial trial was conducted to investigate the initial distribution of inclusions in the steel. A three-dimensional multiphase mathematical model for the collision, transport, and removal of inclusions was then established to simulate the inclusions distribution in the molten steel during the RH process.

## II. INDUSTRIAL TRIALS TO INVESTIGATE INCLUSIONS IN THE MOLTEN STEEL

### A. Methodology

An industrial trial was conducted to investigate the initial distribution of inclusions in an Interstitial Free (IF) steel during the RH refining. The scheme of the trial is illustrated in Figure 2. The refining sustained 45 minutes, which consisted of three periods. The first five minutes was used to warm up the molten steel to raise the temperature of the steel from  $1587^\circ\text{C}$  to  $1650^\circ\text{C}$ . The vacuum suction began at the 5 minutes and persevered for 15 minutes, when the decarburization of the molten steel was also executed. Aluminum was added into the steel at 20 minutes in order to compensate the heat loss of the steel during the refining. The

circulation under deep vacuum kept on for 10 minutes. After the deep vacuum, the vacuum was broken at 30 minutes, followed by a 15-minutes standing. The temperature of the steel was about 1610 °C after the deep vacuum. Seven steel samples were taken during the circulation and the standing process.

Steel samples were cut into cubes and inlaid using the epoxy. After the grinding and polishing, inclusions in the polished section were analyzed employing an automatic scanning electron microscopy equipped with an energy-dispersive spectroscopy (SEM–EDX).

### B. Inclusions Distribution

Typical  $\text{Al}_2\text{O}_3$  inclusions in IF steels are shown in Figure 3. Inclusions in the steel were pure  $\text{Al}_2\text{O}_3$  due to the aluminum deoxidation. Alumina inclusions were in shape of polymer or clusters, and single  $\text{Al}_2\text{O}_3$  inclusions were seldom detected, which indicated that the collision and coalescence of inclusions occurred quite frequently during the refining.

The aggregated  $\text{Al}_2\text{O}_3$  inclusions would further agglomerate into large  $\text{Al}_2\text{O}_3$  clusters as the collision continued, which could be hundreds of micrometers in diameter, as shown in Figure 4. The  $\text{Al}_2\text{O}_3$  clusters could even reach the centimeter-size level, as Figure 4(b) shows. These large clusters had detrimental effect on the property of the steel, so that controlling the collision and agglomeration of  $\text{Al}_2\text{O}_3$  inclusions was quite essential in the production of IF steels.

To obtain a statistically plausible distribution of inclusions, the analyzed area was larger than  $700 \text{ mm}^2$ , so that a large number of inclusions were detected. Steel samples were gridded and polished three times with a thickness of 0.5 mm for each layer. Then a three-dimensional distribution of inclusions was analyzed and obtained, as shown in Figure 5. There were inclusions with diameter larger than  $10 \mu\text{m}$  in all of the three layers, indicating an approximately random distribution of inclusions in the steel.

The obtained distribution of inclusions was in two-dimensional, which could not be used as the initial distribution for the numerical simulation. According to the stereology,<sup>[35]</sup> the three-dimensional distribution of inclusions could be calculated from the two-dimensional distribution using the following equations.

$$C_{2D} = \frac{N_{2D}}{A_{\text{detected}}} \quad [1]$$

$$C_{3D} = \frac{C_{2D}}{d_{\text{inc}}} \quad [2]$$

where  $C_{2D}$  is the number density of inclusions in two-dimensional,  $\#/m^2$ ;  $C_{3D}$  is the number density of inclusions in three-dimensional,  $\#/m^3$ ;  $N_{2D}$  is the detected quantity of inclusions in polished sections, #;  $A_{\text{detected}}$  is the total area of detected sections,  $m^2$ ;  $d_{\text{inc}}$  is the diameter of inclusions, m.

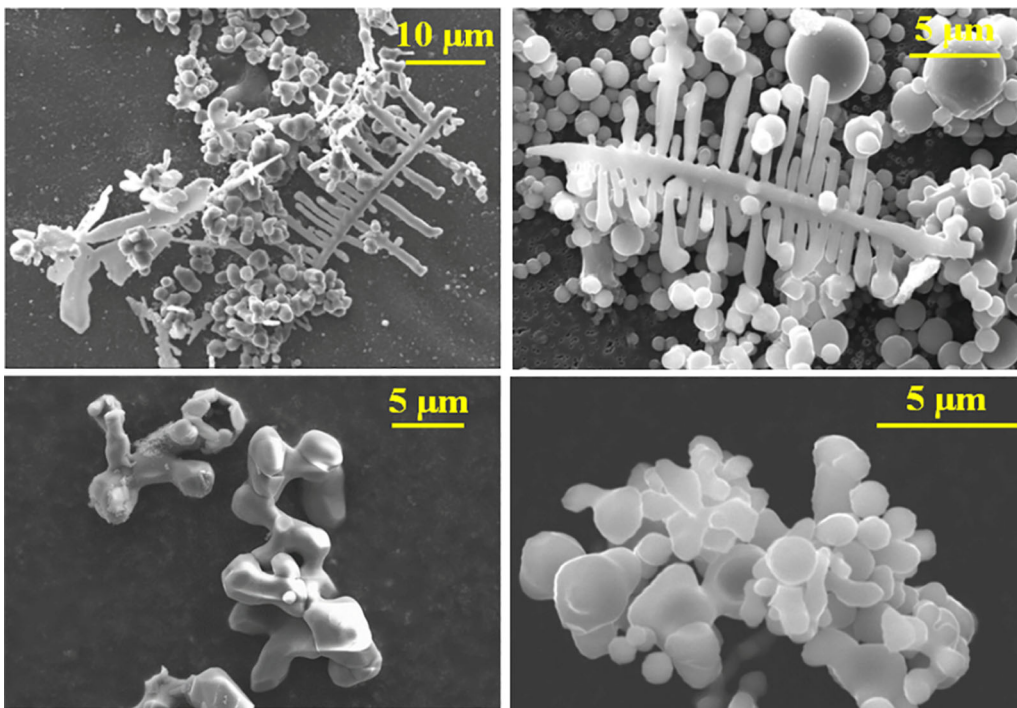


Fig. 3—Typical  $\text{Al}_2\text{O}_3$  cluster inclusions extracted from Al-killed steels. (The first, second, and the last images were reprinted with permission from Ref. [34]).

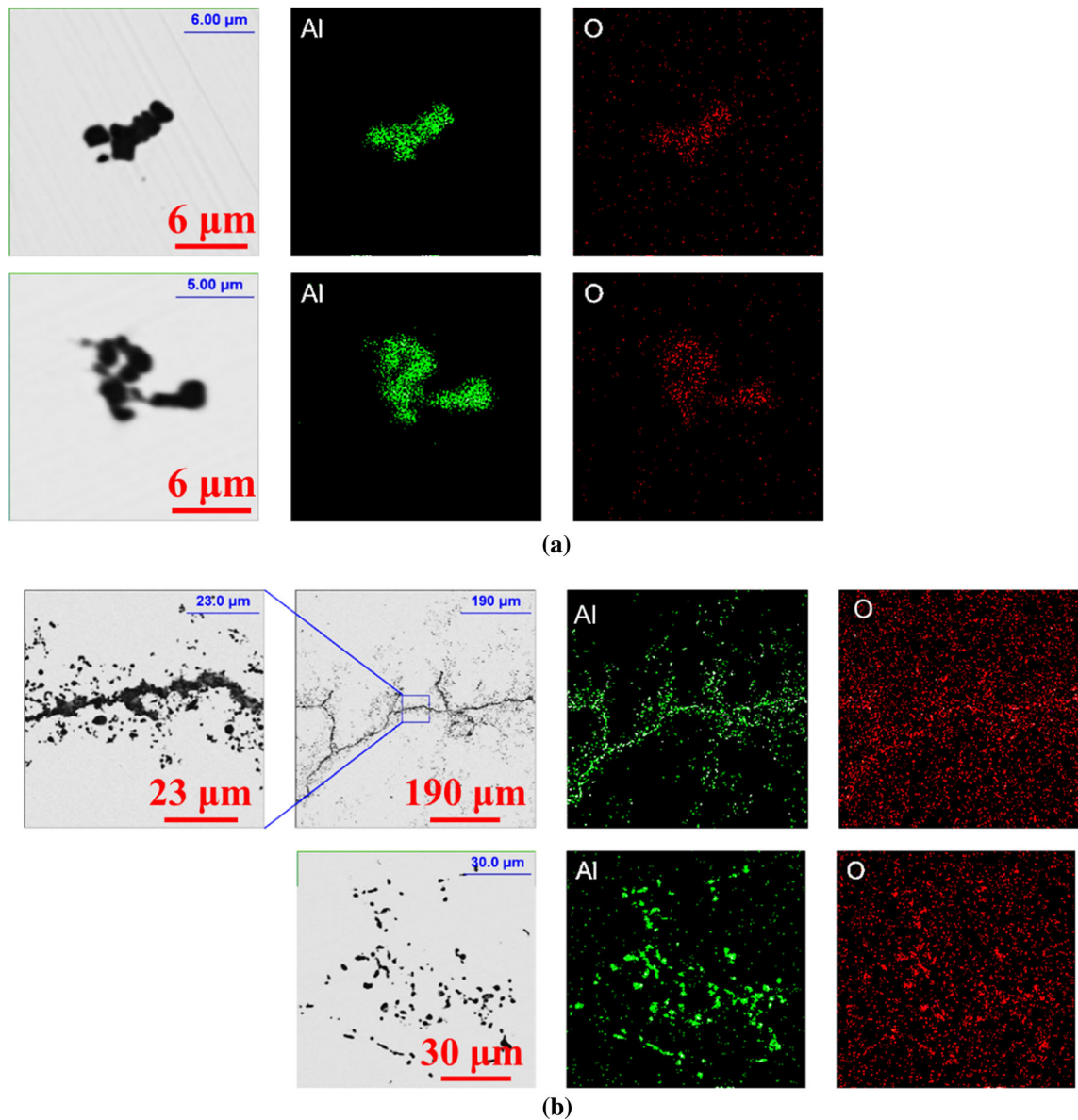


Fig. 4—Morphology and element mapping of (a) aggregated  $\text{Al}_2\text{O}_3$  and (b)  $\text{Al}_2\text{O}_3$  clusters inclusions in the steel.

The size distribution of inclusions in the steel after adding aluminum for 2 minutes was applied as the initial size distribution for the following numerical simulation, as shown in Figure 6. The group interval for histograms in Figure 6 was  $1.0 \mu\text{m}$ . With the increase of inclusions diameter, the number density decreased rapidly. The number density of inclusions with diameter smaller than  $1 \mu\text{m}$  was closed to  $1 \times 10^{15} \text{ \#}/\text{m}^3$ , while that for inclusions with diameter larger than  $10 \mu\text{m}$  was less than  $1 \times 10^{10} \text{ \#}/\text{m}^3$ . The appearance of large inclusions was accidental. Therefore, inclusions were absent for some size groups, such as those with diameter between  $14$  and  $15 \mu\text{m}$  and  $27$ – $36 \mu\text{m}$ .

### III. NUMERICAL MODEL FOR THE FLUID FLOW AND INCLUSIONS DISTRIBUTION

#### A. Three-Dimensional Multiphase Fluid Flow

A coupled discrete particle model (DPM) and volume of fluid (VOF) model were applied to simulate the motion of injected argon bubbles and track the steel–air interface during the RH process. Besides, the  $k$ – $\epsilon$  two-equation turbulent model was employed to solve the turbulent flow field. The detailed description and validation of these models have been discussed thoroughly elsewhere.<sup>[2,36]</sup> Herein, only main governing equations are listed as follows.

Continuity equation (VOF model):

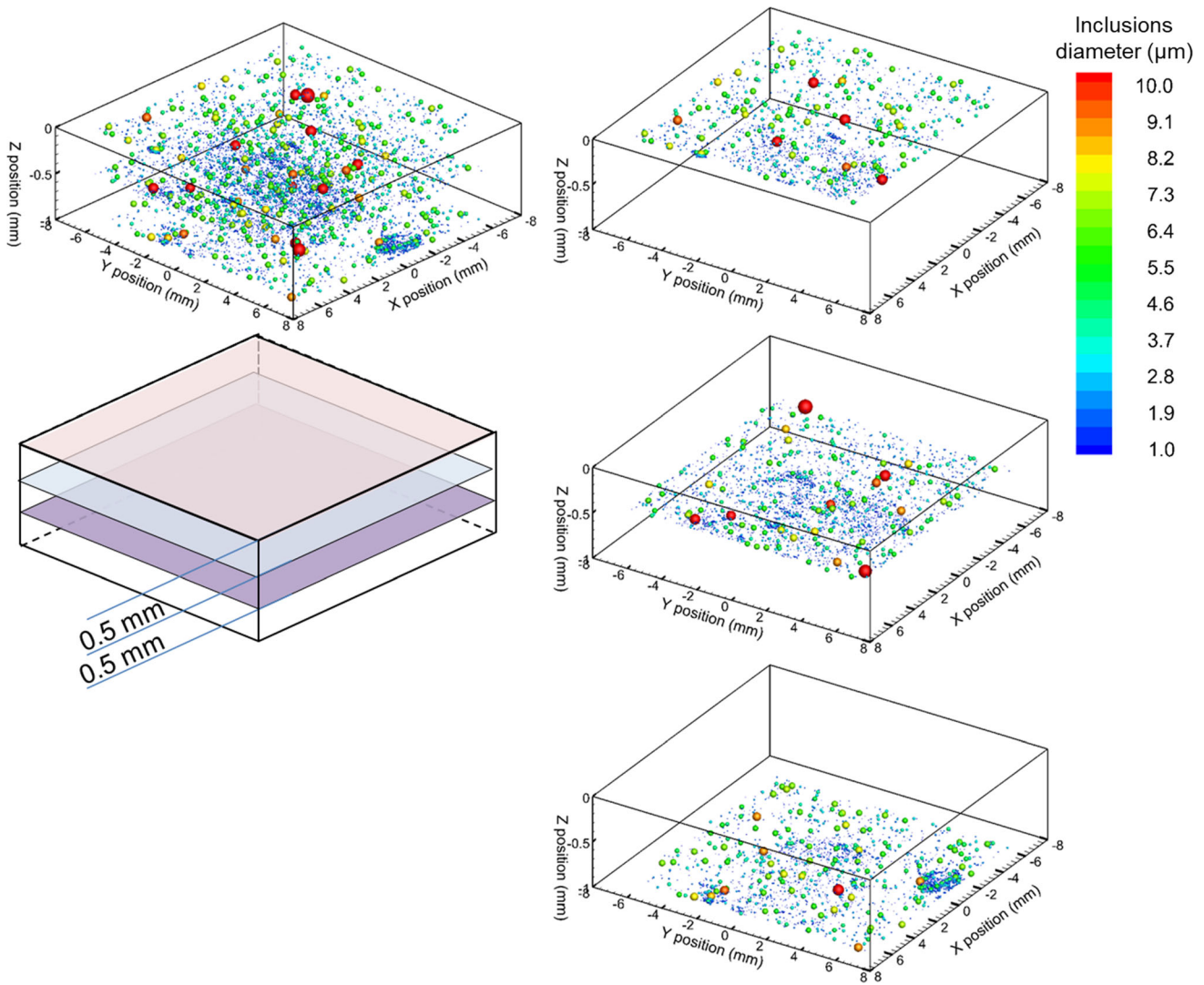


Fig. 5—Three-dimensional spatial distribution of inclusions in a steel sample.

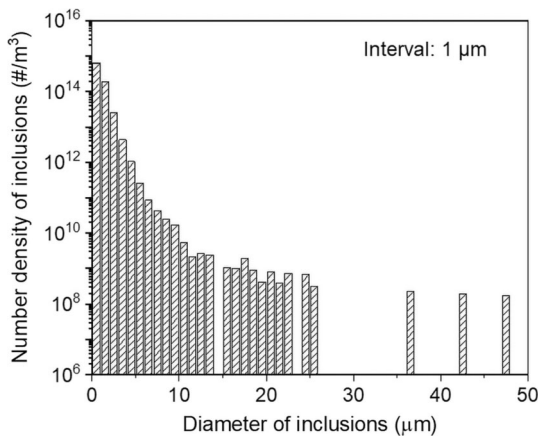


Fig. 6—Three-dimensional number density transformed from two-dimensional measurement of inclusions in the steel after adding aluminum for 2 min.

$$\frac{\partial f_q \rho_q}{\partial t} + \nabla \cdot (f_q \rho_q \vec{u}_q) = 0 \quad [3]$$

Momentum conservation equation (VOF model):

$$\frac{\partial}{\partial t} (\rho_M \vec{u}_M) + \nabla \cdot (\rho_M \vec{u}_M \vec{u}_M) = -\nabla p + \nabla \cdot [\mu_M (\nabla \vec{u}_M + \nabla \vec{u}_M^T)] + \rho_M \vec{g} + \vec{F} \quad [4]$$

Turbulence equations ( $k$ - $\varepsilon$  two-equation model):

$$\frac{\partial \rho_M k}{\partial t} + \nabla \cdot (\rho_M \vec{u}_M k) = \nabla \cdot \left[ \left( \mu_M + \frac{\mu_{t,M}}{\sigma_k} \right) \nabla k \right] + G_k - \rho_M \varepsilon + S_k \quad [5]$$

$$\frac{\partial \rho_M \varepsilon}{\partial t} + \nabla \cdot (\rho_M \vec{u}_M \varepsilon) = \nabla \cdot \left[ \left( \mu_M + \frac{\mu_{t,M}}{\sigma_\varepsilon} \right) \nabla \varepsilon \right] + \frac{\varepsilon}{k} (C_{1\varepsilon} G_k - C_{2\varepsilon} \rho_M \varepsilon) + S_\varepsilon \quad [6]$$

The motion of argon bubbles (DPM):

$$\frac{d\vec{u}_B}{dt} = \vec{F}_D + \vec{F}_G + \vec{F}_B + \vec{F}_{VM} + \vec{F}_P + \vec{F}_L \quad [7]$$

where  $f_q$  is the volume fraction of the  $q$ th phase;  $\rho_q$  and  $\rho_M$  are the density of the  $q$ th phase and the mixture phase, kg/m<sup>3</sup>;  $t$  is time, s;  $u_q$  and  $u_M$  are the velocity of the  $q$ th phase and the mixture phase, m/s;  $p$  is the static pressure, Pa;  $\mu_M$  and  $\mu_{t,M}$  are the molecular viscosity and turbulent viscosity of the mixture phase, kg/(m s);  $g$  is the gravitational acceleration, m/s<sup>2</sup>;  $\vec{F}$  is the source term caused by argon bubbles for the momentum, kg/(m<sup>2</sup> s<sup>2</sup>);  $k$  is the turbulent kinetic energy, m<sup>2</sup>/s<sup>2</sup>;  $\sigma_k$  and  $\sigma_\varepsilon$  are the turbulent Prandtl numbers for  $k$  and  $\varepsilon$ ;  $G_k$  is the generation of  $k$  due to the mean velocity gradients, kg/(m s<sup>2</sup>);  $\varepsilon$  is the dissipation rate for  $k$ , m<sup>2</sup>/s<sup>3</sup>;  $S_k$  and  $S_\varepsilon$  are source terms for the  $k$  and  $\varepsilon$ ;  $C_{1\varepsilon}$  and  $C_{2\varepsilon}$  are constants; and terms in the right-hand of Eq. [7] represent the acceleration due to the drag force, gravitational force, buoyancy force, virtual mass force, pressure gradient force, and lift force, respectively, m/s<sup>2</sup>.

### B. Collision, Transport, and Removal of Inclusions

The concentration (number density) field of inclusions in the steel was simulated by solving the transport equation of the number density of inclusions, as shown in Eq. [8], where only the transport in the molten steel was considered as inclusions were assumed to exist in the steel merely.

$$\frac{\partial}{\partial t} (\rho_{st} C) + \nabla \cdot (\rho_{st} \vec{u}_{inc} C) = \nabla \cdot \left( \frac{\mu_{eff}}{Sc_t} \nabla C \right) + S_C \quad [8]$$

where  $C$  is the concentration (number density) of inclusions, #/m<sup>3</sup>;  $\vec{u}_{inc}$  is the velocity of inclusions, the value in gravitational direction was equal to the value of the steel velocity plus the Stokes velocity of inclusions, as shown in Eq. [9], m/s;  $\mu_{eff}$  is the effective turbulent viscosity, which was calculated using Eq. [10],<sup>[12,23,37,38]</sup> kg/(m s);  $Sc_t$  is the turbulent Schmidt number, 0.7;<sup>[28]</sup> and  $S_C$  is the source term for the number density of inclusions due to the collision.

$$\vec{u}_{inc} = \vec{u}_{st} + U_{stokes} \vec{e}_z = \vec{u}_{st} + \frac{g \cdot (\rho_{st} - \rho_{inc}) \cdot d_{inc}^2}{18\mu_{st}} \vec{e}_z \quad [9]$$

$$\mu_{eff} = \mu_{st} + \mu_t = \mu_{st} + C_\mu \rho_{st} \frac{k^2}{\varepsilon} \quad [10]$$

where subscripts “inc” and “st” represent inclusions and steel;  $\vec{e}_z$  is the unit vector in  $z$  direction;  $C_\mu$  is constant, 0.09.<sup>[39]</sup>

Two types of collision between inclusions, turbulent collision and Stokes collision, were considered in the current study. The Brownian collision was ignored as the rate of Brownian collision was much lower than the other two collisions as for inclusions with diameter was greater than 1  $\mu\text{m}$ .<sup>[9,26]</sup> Therefore, the source term in Eq. [8],  $S_C$ , was calculated as follows.

$$\frac{S_{Ck}}{\rho_{st}} = \frac{2V_{k-1}}{V_k} \beta_{k-1,k-1} C_{k-1} C_{k-1} + \sum_{i=1}^{k-1} \frac{V_i}{V_k} \beta_{i,k} C_i C_k - \sum_{i=k}^{\max} (1 + \delta_{ik}) \beta_{i,k} C_i C_k \quad [11]$$

where  $V_k$  is the volume of the  $k$ th group inclusions, m<sup>3</sup>;  $\beta_{i,k}$  is the collision frequency between the  $i$ th and  $k$ th group inclusions, which was calculated using Eq. [12], #/(m<sup>3</sup> s);  $\delta_{ik}$  is the Kronecker’s delta function,  $\delta_{ik} = 1$  for  $i = k$  and  $\delta_{ik} = 0$  for  $i \neq k$ .

$$\beta_{i,j} = \beta_{Si,j} + \beta_{Ti,j} = \frac{2\alpha g \pi (\rho_{st} - \rho_{inc})}{9\mu_{st}} \cdot (r_i + r_j)^3 \cdot |r_i - r_j| + 1.3\alpha \sqrt{\pi} (r_i + r_j)^3 \left( \frac{\rho_{st} \varepsilon}{\mu_{st}} \right)^{0.5} \quad [12]$$

$$\alpha = 0.738 \left[ \frac{\mu_{st} (\min(r_i, r_j))^3 (\rho_{st} \varepsilon / \mu_{st})^{0.5}}{H_{inc}} \right]^{-0.242} \quad [13]$$

where  $r$  is the radius of inclusions, m;  $\alpha$  is the coagulation probability for the collision;  $H_{inc}$  is the Hamaker constant for inclusions, J.

In order to make the computation feasible, the particle-size-grouping (PSG) method<sup>[4]</sup> was employed to solve population balance equations for the collision process of inclusions. As the maximum diameter of inclusions was in the range of 40 to 50  $\mu\text{m}$ , which was in the 14th group, considering the coverage of inclusions, two more groups were adopted, that was, inclusions were divided into 16 groups, from 1 to 115.1  $\mu\text{m}$ . Each group had a diameter range and a characteristic diameter to represent all inclusions within the corresponding diameter range. Thereby, the diameter of the  $k$ th group inclusions was calculated as follows.

$$d_{inc,k} = d_{inc,1} 2.5^{\frac{k-1}{3}} \quad [14]$$

Generally, the density of inclusions was less than that of the molten steel so that inclusions were floated by the buoyancy force,<sup>[5]</sup> which lead to the removal of inclusions. Inclusions were considered to be removed once they moved to the top slag surface in the ladle. The top slag surface was defined as where the volume of steel was less than 0.185 in the ladle. An annihilation condition for inclusions was employed to calculate the inclusions removal at the steel–slag interface.

It should be noted that the removal of inclusions was assumed to only occurred at the top slag of the ladle, since there was little slag at the top surface in the vacuum chamber of the RH. Figure 7 illustrates the schematic of the model.

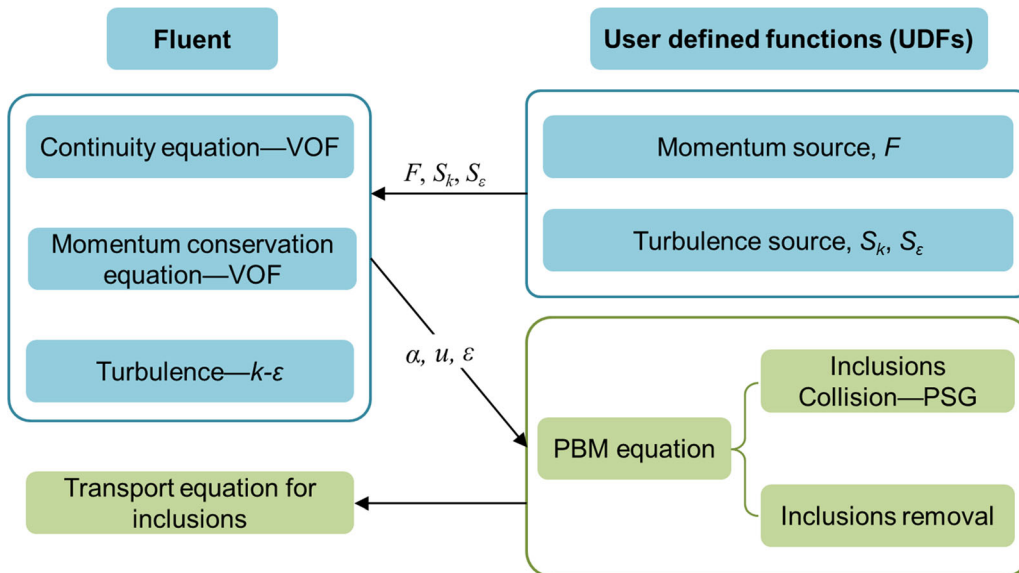


Fig. 7—Schematic of the coupled models used in the current study.

### C. Computational Scheme and Boundary Conditions

The mesh and boundary conditions used in the current study are shown in Figure 8. Top surfaces of the chamber and the ladle were the pressure outlet condition, and the side of the chamber and the ladle was no-slip wall boundary condition. The total quantity of structured cells was approximately 540,000. Figure 8(b) shows the schematic for the twelve argon blowing orifices that the argon gas at a total flow rate of 3000 NL/min was blown from. The diameter of these orifices was six millimeter. After the steady flow field was obtained, transport equations of inclusions were solved in the molten steel domain, and global mean number densities for each group of inclusions were monitored and output, which were calculated as shown in Eq. [15].

$$\bar{C}_k = \frac{\sum_i^{\text{All}} C_{k,i} f_{\text{st}} V_{i,\text{cell}}}{\sum_i^{\text{All}} f_{\text{st}} V_{i,\text{cell}}} \quad [15]$$

where  $V_{i,\text{cell}}$  is the volume of a single cell in the calculation domain,  $\text{m}^3$ .

As inclusions in the steel were divided into 16 groups according to diameters, a new number density distribution of each group inclusions is shown in Figure 9 based on Figure 6. The width of the bars in Figure 9 represents the range of inclusions diameter in a certain group, indicating that the group with bigger index had a wider range of diameter. The diameter of the largest inclusions was in the range of 46.04 to 62.49  $\mu\text{m}$ , the number density of which was  $5.90 \times 10^7 \text{ \#}/\text{m}^3$ . Other parameters used in the simulation are listed in Table I.

## IV. MULTIPHASE FLUID FLOW AND INCLUSIONS DISTRIBUTION WITH ARGON FLOW RATE OF 3000 NL/MIN

### A. Fluid Flow of the Molten Steel

The model for the fluid flow of the molten steel had been validated in former studies,<sup>[2,7,36,40]</sup> so that the validation for fluid flow models was not discussed in the current work. The calculated speed, streamlines, turbulent energy, and turbulent energy dissipation rate of the molten steel are shown in Figure 10. The molten steel in the down-leg had greater speed, turbulent energy, and turbulent energy dissipation rate. The speed of the molten steel in the ladle was lower than 0.42 m/s, except the impingement zone by the steel flow in the down-leg, where the speed of the steel was faster than 0.6 m/s. Streamlines in Figure 10(b) show that the molten steel in the ladle converged to the up-leg and poured into the vacuum chamber. The steel then rushed from the down-leg to the ladle bottom and spread inside the ladle. The turbulent energy and turbulent energy dissipation rate had a similar distribution. Overall, the flow of the steel in the ladle was much weaker than that in the chamber.

Figures 11 and 12 are the speed and vector of the molten steel on two top surfaces, which are in the chamber and ladle, respectively. These two surfaces were set to be iso-surface of the steel volume fraction with a value of 0.9. The top surface of the steel in the chamber was not a plane, where the fluctuation of the steel was quite violent, which was often ignored in published literature.<sup>[7,14,32,33]</sup> In the top surface of the steel in the chamber, the zone on the top of the up-leg was apparently higher than that of the down-leg. The speed was the highest at the area where the steel fell from the height to the ground. The vector of the top surface in the chamber indicated that the steel moved

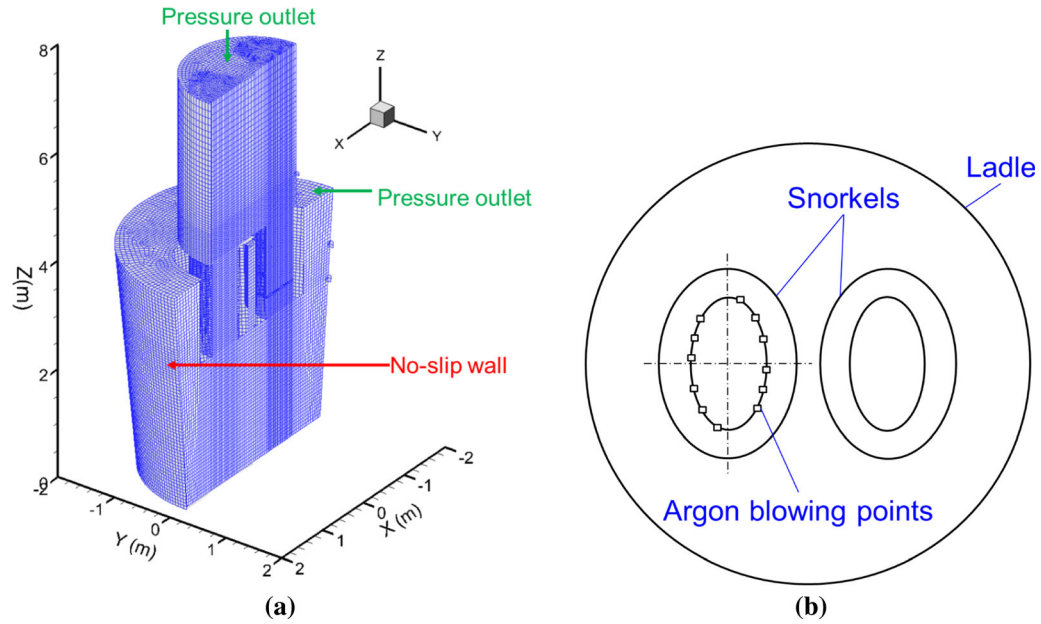


Fig. 8—(a) Mesh, boundary conditions and (b) argon blowing points used for the current RH numerical modeling.

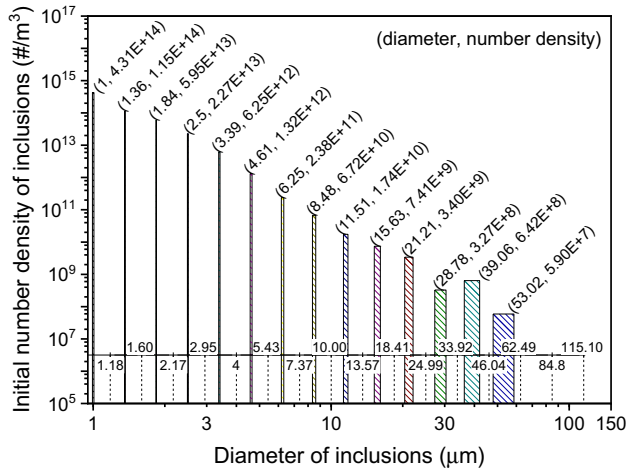


Fig. 9—Initial number density of inclusions in the molten steel.

from the top of the up-leg to the up-leg. The free surface in the ladle was very smooth with litter fluctuation, which was different from the top surface in the chamber. The speed at the free surface was rather slower than that in the chamber.

### B. Model Validation for Inclusions Distribution: Evolution of the Total Oxygen in the Steel

As inclusions in the molten steel were mostly  $\text{Al}_2\text{O}_3$  due to the aluminum deoxidation, the total oxygen (T.O) in the molten steel was employed to represent the population of inclusions. Equation [16] shows the conversion formula from the population of inclusions into the T.O content.

$$\text{T.O (ppm)} = \sum_i^{\text{All}} C_i V_i \frac{3\rho_{\text{Al}_2\text{O}_3} M_{\text{O}}}{\rho_{\text{st}} M_{\text{Al}_2\text{O}_3}} \times 10^6 \quad [16]$$

where  $M_{\text{O}}$  and  $M_{\text{Al}_2\text{O}_3}$  are the molar mass of O and  $\text{Al}_2\text{O}_3$ , kg/mol.

The measured and simulated T.O contents are shown in Figure 13. Under the current removal condition, the T.O content decreased from 251 to 93 ppm in approximately 10 minutes, which was in good agreement with measured ones. The T.O after refining for 1800 seconds was approximately 14 ppm. With the refining continued, the decrease rate of the T.O became slower and slower. In the first 300 seconds, the decrease of the T.O was 100 ppm, while that in next several 300 seconds was 59, 36, 22, 13, and 8 ppm, respectively.

### C. Removal Fraction of Inclusions from the Steel

Inclusions sustained to be removed from the molten steel at the free surface in the ladle, which was defined as the iso-surface of volume fraction of the steel phase with value of 0.185. The population decrease of a certain size group inclusion was composed of two part, the removal at the free surface and the change due to the collision. Considering that the collision between inclusions had no effect on the total volume of inclusions, the decrease in the total volume of inclusions was defined as the removal fraction of inclusions, as shown in Eq. [17]. The removal rate was also calculated, as defined in Eq. [18].

$$\eta_t = \frac{\sum_{i=1}^{\text{All}} V_{i,0} C_{i,0} - \sum_{i=1}^{\text{All}} V_{i,t} C_{i,t}}{\sum_{i=1}^{\text{All}} V_{i,0} C_{i,0}} \times 100 \text{ pct} \quad [17]$$



**Table I. Parameters Used in the Current Study**

Parameter	Value	References
Steel		
Density, kg/m <sup>3</sup>	7020	24
Molecular Viscosity, kg/(m s)	0.0067	
Argon		
Density, kg/m <sup>3</sup>	1.783	20
Interface Force from the Molten Steel, N/m	1.5	
Inclusions		
Density, kg/m <sup>3</sup>	3500	24
Hamaker Constant in the Molten Steel, J	$2.3 \times 10^{-20}$	

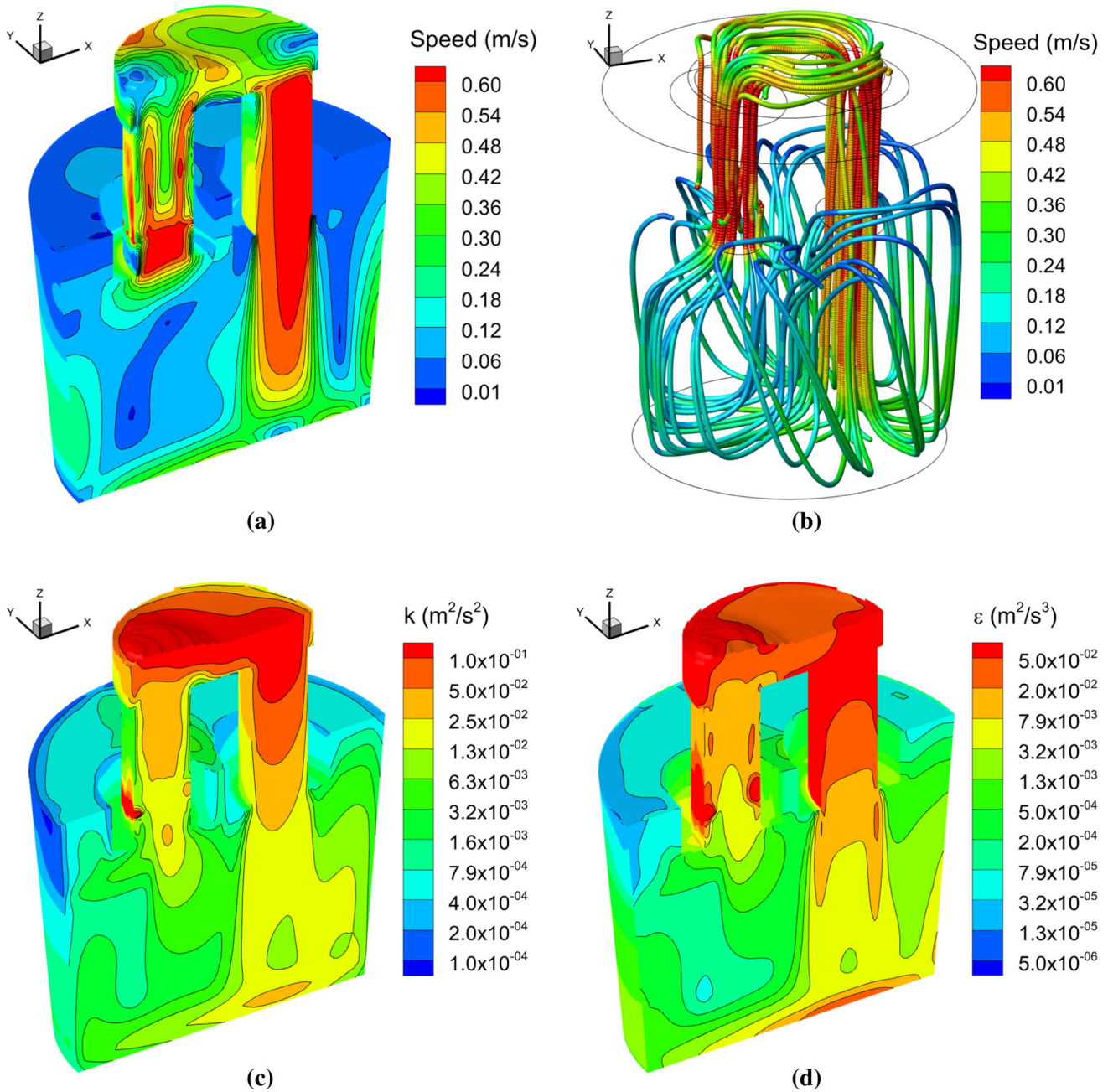


Fig. 10—(a) speed, (b) streamlines, (c) turbulent energy, and (d) turbulent energy dissipation rate of the molten steel in the RH furnace.

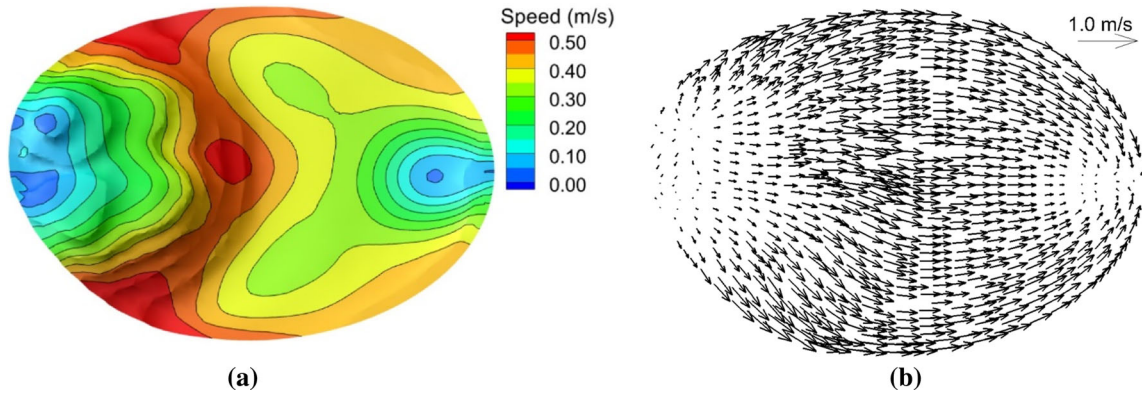


Fig. 11—(a) Fluid flow speed and (b) vector of the molten steel on the top surface of the molten steel in the vacuum chamber of the RH refining.

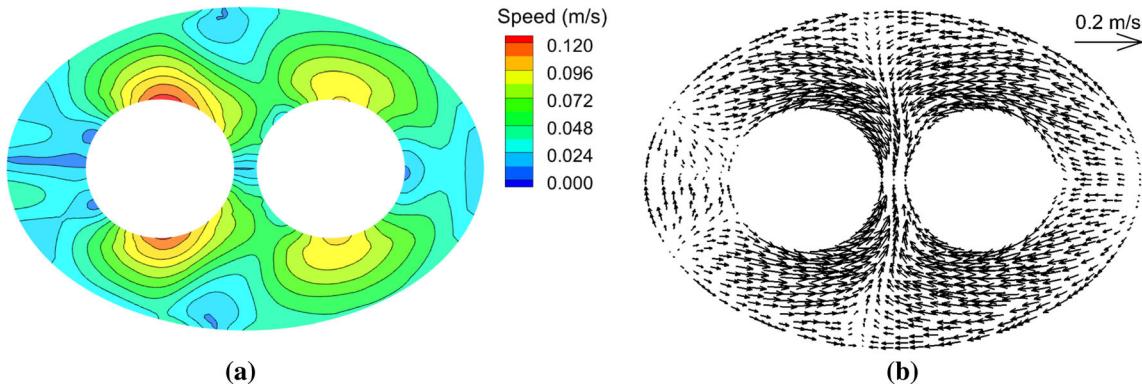


Fig. 12—(a) Fluid flow speed and (b) vector of the molten steel on the free surface of the molten steel in the ladle.

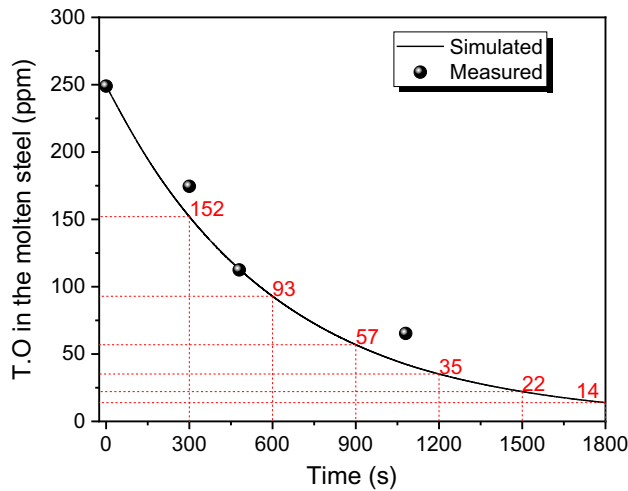


Fig. 13—Variation of the measured total oxygen in the molten steel.

$$v_{\eta} = \frac{d\eta}{dt} \quad [18]$$

where  $\eta_t$  is the removal fraction of inclusions at the time of  $t$ , pct;  $v_{\eta}$  is the removal rate of inclusions, pct/s.

Figure 14 shows the cumulative removal fraction and the removal rate of inclusions. The evolution of the removal fraction shows an opposite regularity to the evolution of the T.O. The removal fraction increased with the refining time, but the removal rate showed a decrease with the refining time. The removal rate at the very beginning was the highest, with a value bigger than 0.2 pct/s. A litter fluctuate was revealed before 300 seconds during the refining, which was caused by the centered difference formula employed in the current study to approximate the removal rate from the cumulative removal fraction. The removal rate dropped down sharply with the refining continued. When refining for 300 seconds, the removal rate decreased to less than 0.1 pct/s. The removal fraction at 1800s was larger than 90 pct, indicating a high efficiency of the RH refining in removing inclusions.

#### D. Evolution of Global Characteristics of Inclusions

The global mean number density of inclusions was calculated using Eq. [15], and the results of sixteen size groups of inclusions are shown in Figure 15. Since inclusions with small diameter were more likely to collide into larger inclusions, the number density of small inclusions ( $d_1-d_3$ ) decreased more sharply than large inclusions. However, for inclusions with diameter larger than  $2.5 \mu\text{m}$  ( $d_4-d_{16}$ ), the number density had an increase

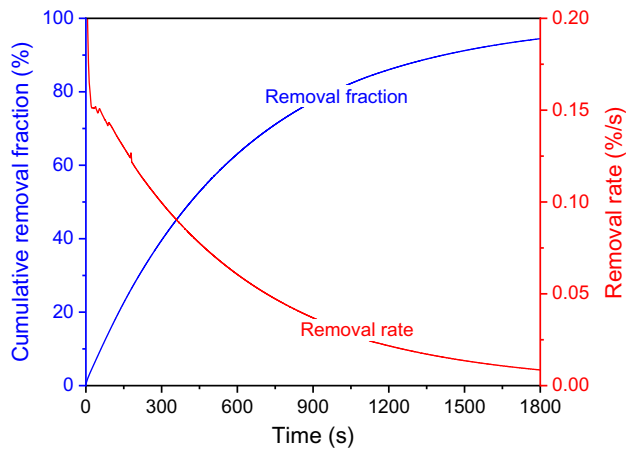


Fig. 14—Simulated removal fraction and removal rate of inclusions in the molten steel.

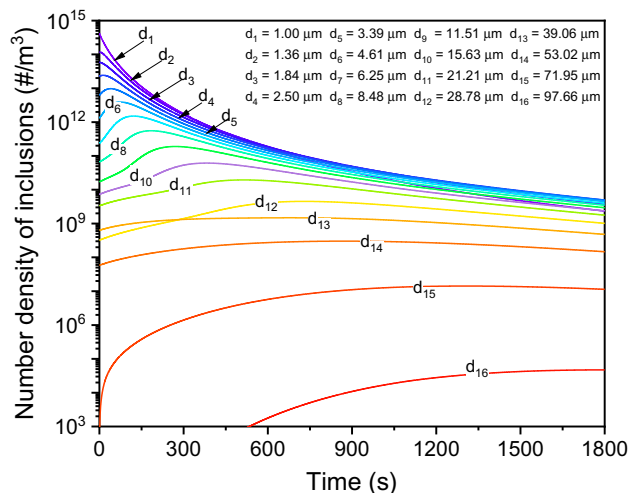


Fig. 15—Evolution of the number density of inclusions of different size groups with refining time.

at the beginning, followed by a continuous decrease. Number densities of all inclusions kept decreasing after a long time of the refining, regardless of the inclusions size. The distribution of number density of inclusions with different diameters after colliding for 0, 300, 600, 1200, and 1800 seconds is shown in Figure 16. Small inclusions accounted for the majority before the collision. When colliding for 300 seconds, the number density of inclusions with diameter smaller than  $2.5 \mu\text{m}$  ( $d_1$ – $d_4$ ) had an apparent decrease, which declined from  $10^{13}$  to  $10^{15} \text{ #/m}^3$  into  $10^{12} \text{ #/m}^3$ . Inclusions with diameter larger than  $53.02 \mu\text{m}$  ( $d_{15}$  and  $d_{16}$ ) appeared and grew fast after the collision. As the collision continued, number density of inclusions with diameter less than  $4.61 \mu\text{m}$  ( $d_1$ – $d_6$ ) kept dropping down. After colliding for 1800 seconds, the number density of inclusions ranging from  $d_1$  to  $d_{12}$  was on the order of  $10^9 \text{ #/m}^3$ , while large inclusions (such as inclusions in the group  $d_{16}$ ) were at a very low level.

Figure 17 shows the simulated volumetric average diameter of inclusions, which was calculated using Eq. [19]. The initial average diameter of inclusions was approximately  $1.5 \mu\text{m}$ , which increased continuously during the RH refining. After refining for 1800 seconds, the average diameter was  $14 \mu\text{m}$ . It should be noted that the generation of new tiny inclusions and the break-up of inclusions were not considered in the current model. Therefore, the simulated result overestimated the average diameter of inclusions.

$$\bar{d}_{\text{inc}} = \left( \frac{6 \sum_{k=1}^{16} V_k \bar{C}_k}{\pi \sum_{k=1}^{16} \bar{C}_k} \right)^{\frac{1}{3}} \quad [19]$$

### E. Spatial Distribution of Inclusions in the Steel

Due to the effect of the fluid flow, the number density of inclusions in the steel was position-dependent. Taking the group  $d_1$ ,  $d_8$ , and  $d_{15}$  as example, the spatial distribution of inclusions number density in the steel at 300, 600, 1200, and 1800 seconds was evaluated, as

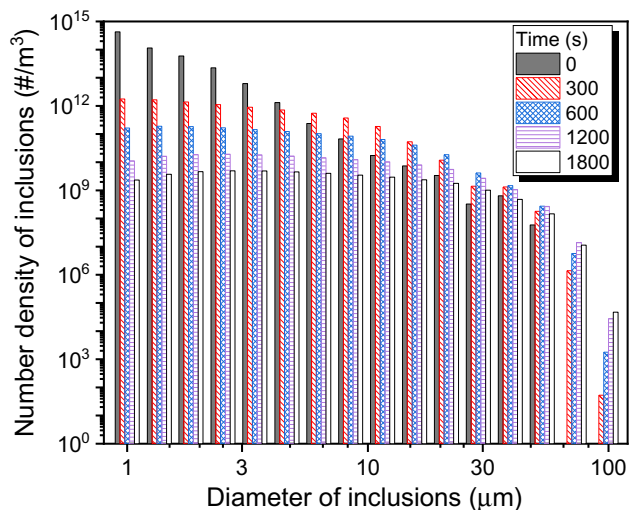


Fig. 16—Size distribution of inclusions after colliding for different times in the molten steel.

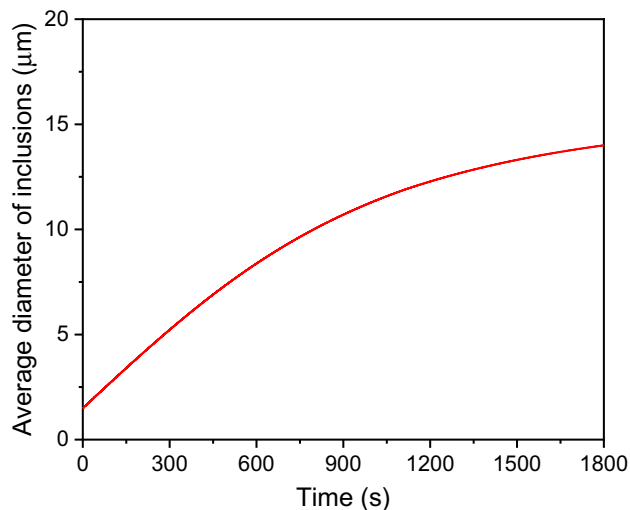


Fig. 17—Simulated average diameter of inclusions in the molten steel with refining time.

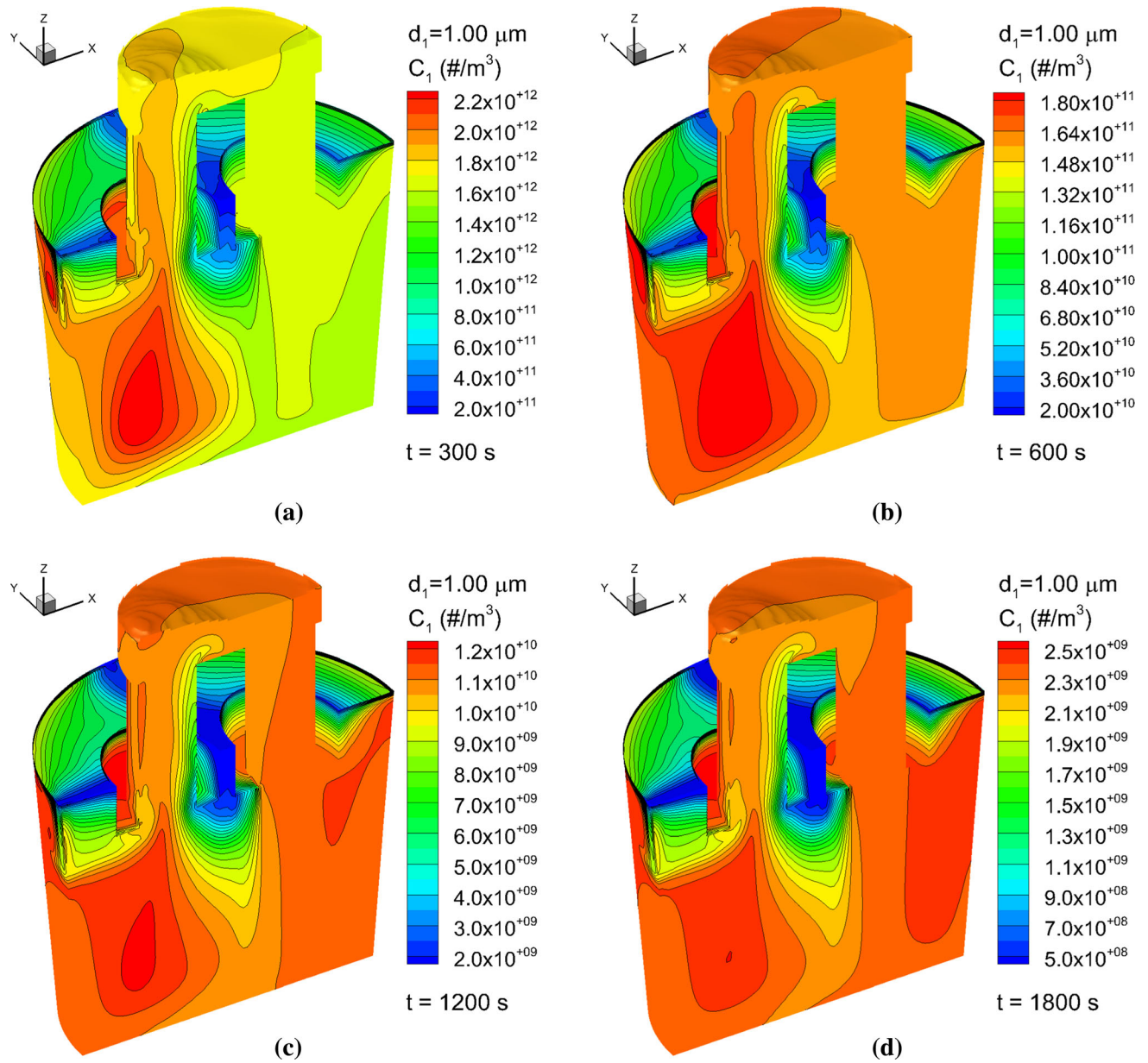


Fig. 18—Spatial distribution of the number density of inclusions with  $d_1 = 1.00 \mu\text{m}$  after certain collision time (a) 300 s, (b) 600 s, (c) 1200 s, (d) 1800 s.

shown in Figures 18 through 20. The original distribution of inclusions was uniformly. After a period of collision, there were significant differences in the number density of inclusions in different regions. For inclusions in group  $d_1$  with diameter of  $1.00 \mu\text{m}$ , the number density of inclusions near the steel surface in the ladle had the minimum value due to the removal boundary condition, while the number density of inclusions near the side wall of the ladle showed a relatively high value. The quantity of inclusions in the middle of two snorkels was quite less than that in other regions in the ladle, which was owing to the frequent circulation of the molten steel in this region, as shown in Figure 10. The number density at 300 s was in the range of  $10^{11}$ – $10^{12}$   $\#/\text{m}^3$ , then dropped to  $10^{10}$ – $10^{11}$   $\#/\text{m}^3$ ,  $10^9$ – $10^{10}$   $\#/\text{m}^3$ , and

$10^8$ – $10^9$   $\#/\text{m}^3$  at 600, 1200, and 1800 seconds, respectively. The spatial distribution of inclusions in group  $d_8$  and  $d_{15}$  showed a similar phenomenon as inclusions in group  $d_1$ .

Figure 21 shows the spatial distribution of T.O in the steel, which was similar to the number density distribution of inclusions. The T.O content ranged in 1 to 16 ppm in different regions in the ladle. In the bulk of the molten steel, the distribution of oxygen showed a symmetry along the plane PP-1 in Figure 21, which was the center plane of two snorkels. The T.O content near the bottom of the ladle was relatively higher than that near the free surface of the ladle. In conjunction with Figure 10, it could be figured out that the content of T.O was high in the region where the flow of the steel was

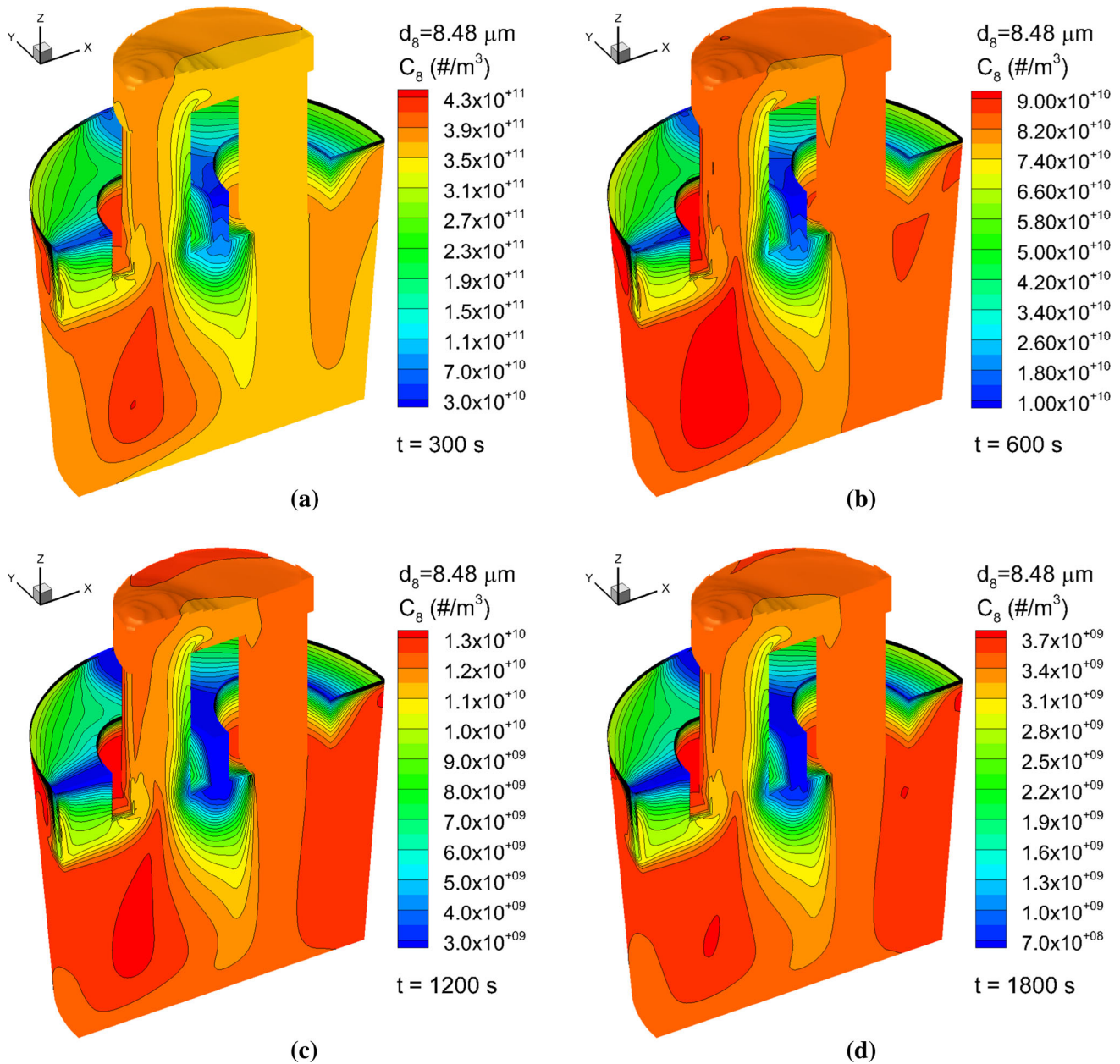


Fig. 19—Spatial distribution of the number density of inclusions with  $d_b = 8.48 \mu\text{m}$  after certain collision time (a) 300 s, (b) 600 s, (c) 1200 s, (d) 1800 s.

very weak, which was the so-called dead zone, owing to the little removal of inclusions in these regions. The gradient of the T.O content in the cross section near the free surface of the ladle was relatively large. In these sections, the T.O content was around 15 ppm on the side, while below 2 ppm in the center. The T.O content in the chamber was in the range of 10 to 15 ppm.

The average diameter of inclusion in the steel also showed an uneven distribution in the steel, though the distinction was little, which was within the scope of 13.95 to 14.15  $\mu\text{m}$ , as shown in Figure 22. The reasons for these differences were the collision and Stokes floatation of inclusions. The collision between inclusions leads to the growth of inclusion, which was related with

the original size of inclusions and the turbulent kinetic energy dissipation rate of the steel flow. However, the effect of the convection term and diffusion term in Eq. [8] was more obvious than that of the growth of inclusions, which resulted in the uniform distribution of the average diameter of inclusions. Overall, the average diameter of inclusions increased slightly from the bottom to the free surface in the ladle, owing to the higher Stokes floatation speed of inclusions with a larger diameter. Besides, an interesting regular was figured out based on simulated results. The average diameter of inclusions was a little large in the area where the total oxygen was small, in particular the region around the outside of the up-leg snorkel in the free surface of the

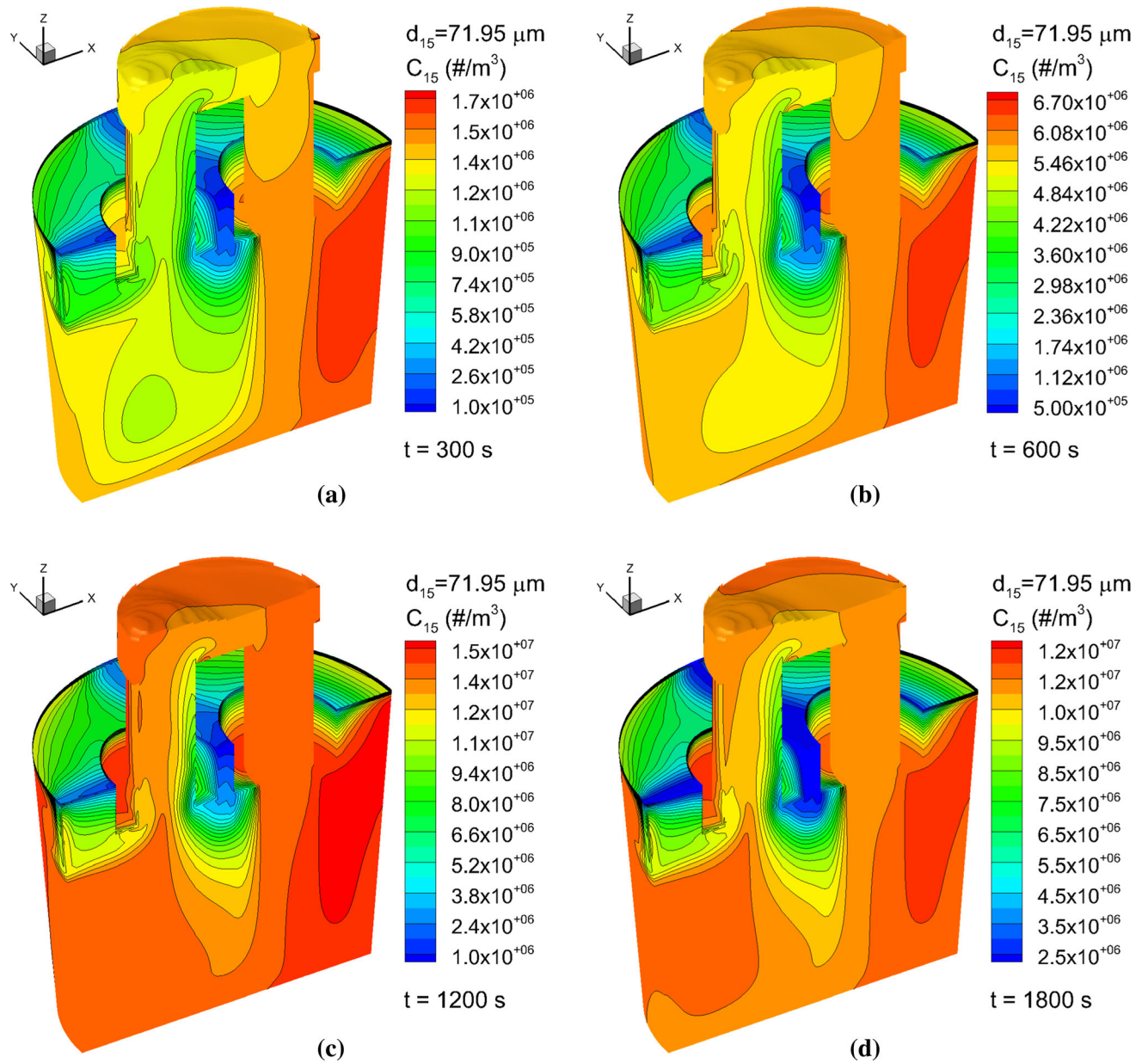


Fig. 20—Spatial distribution of the number density of inclusions with  $d_{15} = 71.95 \mu\text{m}$  after certain collision time (a) 300 s, (b) 600 s, (c) 1200 s, (d) 1800 s.

ladle. The T.O was related the number density of inclusions according to Eq. [16], while the average diameter was determined by the size distribution of inclusions according to Eq. [19]. The removal condition at the free surface led to the minimum of number density of inclusions, resulting in the small content of T.O near the free surface. However, the proportion of large size inclusions in this region was relatively high due to the Stokes floatation of inclusions, resulting in a large average diameter of inclusions.

## V. CONCLUSIONS

In the current study, an industrial trial was conducted to investigate the initial number density distribution of inclusions in the steel, and then, a three-dimensional mathematical model was developed to simulate the fluid flow and inclusions evolution during the RH vacuum refining. Global characteristics and spatial distribution of inclusions in the steel were discussed. The followings are obtained conclusions.

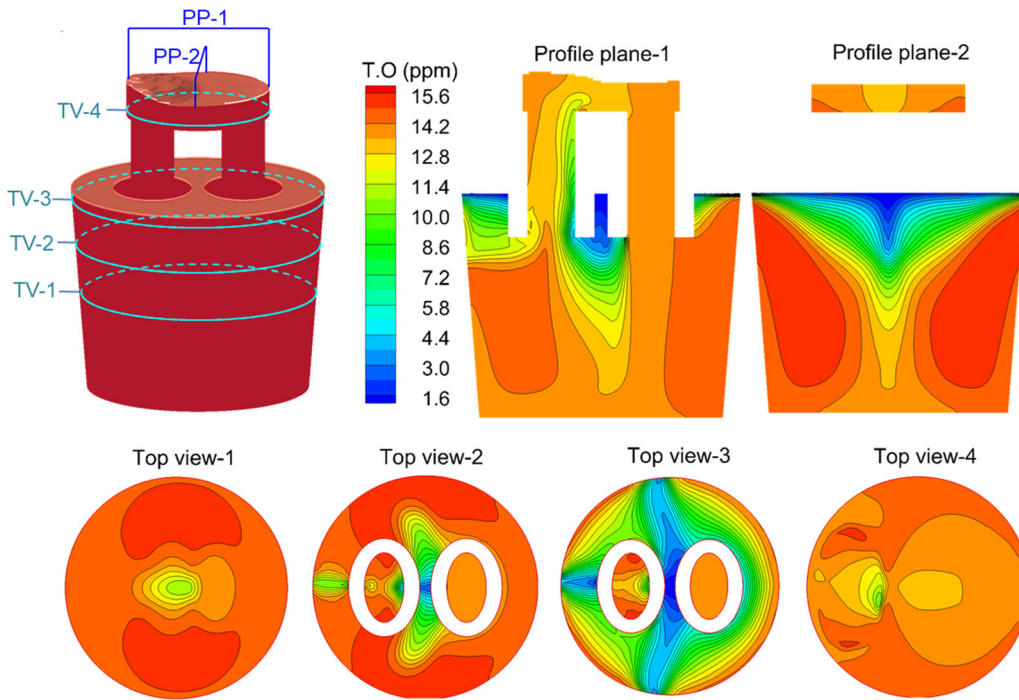


Fig. 21—Spatial distribution of the total oxygen in the molten steel at 1800 s.

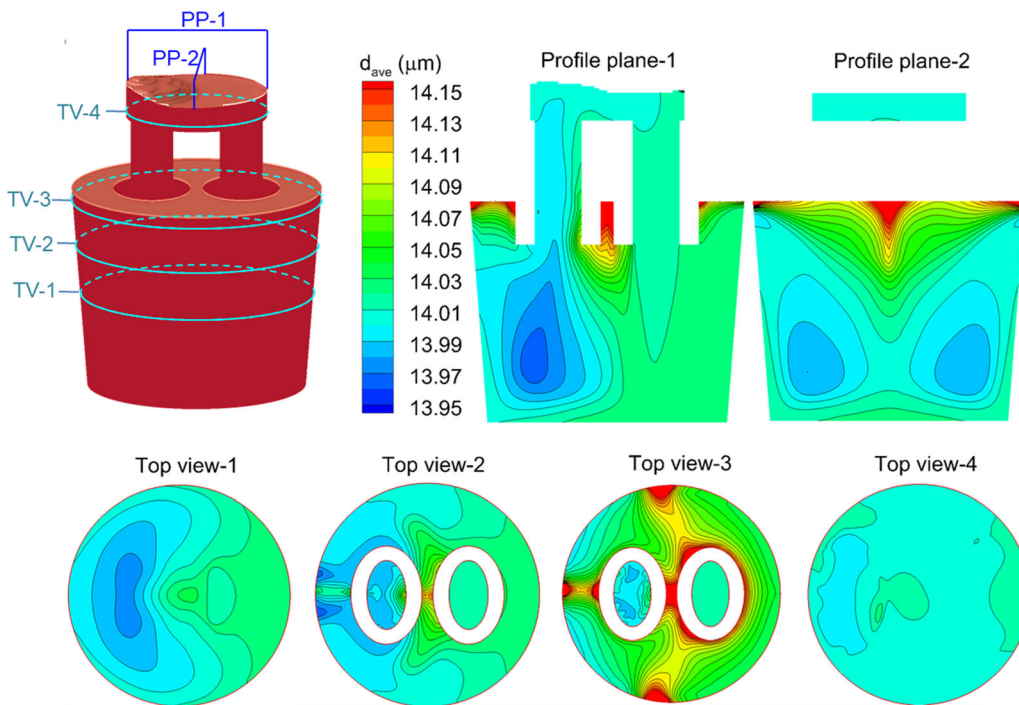


Fig. 22—Spatial distribution of the average diameter of inclusions in the molten steel at 1800 s.

- Inclusions in IF steels were mostly  $\text{Al}_2\text{O}_3$  in aggregations or clusters. The initial number density of inclusions with diameter smaller than  $1\ \mu\text{m}$  was closed to  $1 \times 10^{15}\ \#/\text{m}^3$ , while that with diameter larger than  $10\ \mu\text{m}$  was less than  $1 \times 10^{10}\ \#/\text{m}^3$ .
- The calculated T.O content in the steel decreased from 251 to 93 ppm in approximately 10 minutes, which agreed well with measured ones. With the refining continued, the decrease rate of the T.O became slower and slower. In every 300 seconds, the decrease of the T.O was 100, 59, 36, 22, 13, and 8 ppm, respectively.
- The removal fraction of inclusions increased with the refining time, but the removal rate showed a decrease. The removal rate at the beginning was the highest with a value bigger than 0.2 pct/s, while that decreased to 0.1 pct/s after refining for 300 seconds. The removal fraction at 1800 seconds was larger than 90 pct, indicating a high efficiency of the RH refining in removing inclusions.
- Small inclusions accounted for the majority before the collision. After colliding for 300 seconds, the number density of inclusions with diameter smaller than  $2.5\ \mu\text{m}$  had an apparent decrease, declining from  $10^{13}$  to  $10^{15}\ \#/\text{m}^3$  into  $10^{12}\ \#/\text{m}^3$ .
- The distribution of T.O content in the steel was position-dependent, ranging from 1 to 16 ppm at 1800 seconds. The gradient of the T.O content in the cross section near the free surface of the ladle was relatively large, around 15 ppm on the side and below 2 ppm in the center.
- W.C. Doo, D.Y. Kim, S.C. Kang, and K.W. Yi: *ISIJ Int.*, 2007, vol. 47, pp. 1070–72.
- C. Liu, L. Zhang, F. Li, K. Peng, F. Liu, Z. Liu, Y. Zhao, W. Yang, and J. Zhang: *Steel Res. Int.*, 2021, vol. 92, pp. 2000608. <https://doi.org/10.1002/srin.202000608>.
- H. Ling, C. Guo, A.N. Conejo, F. Li, and L. Zhang: *Metall. Res. Technol.*, 2017, vol. 114, pp. 1–3.
- H. Ling, F. Li, L. Zhang, and A.N. Conejo: *Metall. Mater. Trans. B*, 2016, vol. 47B, pp. 1950–61.
- F. Li, L. Zhang, Y. Liu, and Y. Li: *TMS*, 2014, vol. 2014, pp. 459–66.
- B. Li, Y. Luan, F. Qi, and H. Huo: *J. Northeast. Univ.*, 2005, vol. 26, pp. 759–62.
- K. Shirabe and J. Szekely: *Trans. Iron Steel Inst. Jpn.*, 1983, vol. 23, pp. 465–74.
- D. Geng, H. Lei, and J. He: *ISIJ Int.*, 2012, vol. 52, pp. 1036–44.
- D. Geng, J. Zheng, K. Wang, P. Wang, R. Liang, H. Liu, H. Lei, and J.C. He: *Metall. Mater. Trans. B*, 2015, vol. 46B, pp. 1484–93.
- S. Zheng and M. Zhu: *ICS*, 2015, vol. 2015, pp. 362–65.
- G. Chen, S. He, Y. Li, and Q. Wang: *Ind. Eng. Chem. Res.*, 2016, vol. 55, pp. 7030–42.
- D. Geng, H. Lei, and J. He: *High Temp. Mater. Process.*, 2017, vol. 36, pp. 523–30.
- L. Zhang and F. Li: *JOM*, 2014, vol. 66, pp. 1227–40.
- D. Geng, H. Lei, and J. He: *Metall. Mater. Trans. B*, 2009, vol. 41B, pp. 234–47.
- S. Chen, H. Lei, and M. Wang: *Steel Res. Int.*, 2021, vol. 92, pp. 1–2.
- J. Zhang and H. Lee: *ISIJ Int.*, 2004, vol. 44, pp. 1629–38.
- H. Lei and J. He: *J. Non-Cryst. Solids*, 2006, vol. 352, pp. 3772–80.
- H. Ling and L. Zhang: *JOM*, 2013, vol. 65, pp. 1155–63.
- H. Ling, L. Zhang, and H. Li: *Metall. Mater. Trans. B*, 2016, vol. 47B, pp. 2991–3012.
- L. Zhang and S. Taniguchi: *Int. Mater. Rev.*, 2000, vol. 45, pp. 59–82.
- L. Zhang and B. G. Thomas: *7th European Electric Steelmaking Conference*, 2002, vol. 2, pp. 77–86.
- L. Li, Z. Liu, B. Li, H. Matsuura, and F. Tsukihashi: *ISIJ Int.*, 2015, vol. 55, pp. 1337–46.
- W. Lou and M. Zhu: *Trans. Iron Steel Inst. Jpn.*, 2014, vol. 54, pp. 9–18.
- P.G. Saffman and J.S. Turner: *J. Fluid Mech.*, 1955, vol. 1, pp. 16–30.
- U. Lindborg and K. Torssell: *Trans. Metall. Soc. AIME*, 1968, vol. 242, pp. 94–102.
- G. Chen, S. He, Y. Li, Y. Guo, and Q. Wang: *JOM*, 2016, vol. 68, pp. 2138–48.
- S. Chen, H. Lei, Q. Li, C. Ding, W. Dou, and L. Chang: *JOM*, 2022, vol. 74, pp. 1578–87.
- S. Chen, H. Lei, H. Hou, C. Ding, H. Zhang, and Y. Zhao: *J. Mater. Res. Technol.*, 2021, vol. 15, pp. 5141–50.
- L. Zhang: *Atlas of non-metallic inclusions in steels (I)*, Metallurgical Industry Press, Beijing, 2019, pp. 100–10.
- L. Zhang, B. Rietow, B.G. Thomas, and K. Eakin: *ISIJ Int.*, 2006, vol. 46, pp. 670–79.
- C. Liu, S. Li, and L. Zhang: *Acta Metall. Sin.*, 2018, vol. 54, pp. 347–56.
- W. Lou and M. Zhu: *Metall. Mater. Trans. B*, 2013, vol. 44B, pp. 762–82.
- L. Wang, Q. Zhang, S. Peng, and Z. Li: *ISIJ Int.*, 2005, vol. 45, pp. 331–37.
- H. Duan, Y. Ren, and L. Zhang: *Metall. Mater. Trans. B*, 2019, vol. 50B, pp. 1476–89.
- C. Liu, H. Duan, and L. Zhang: *Metals*, 2019, vol. 9, p. 442.

## ACKNOWLEDGMENTS

The authors are grateful for support from the National Natural Science Foundation of China (Grant No. U22A20171), the High Steel Center (HSC) at North China University of Technology, and the High Quality Steel Consortium (HQSC) at University of Science and Technology Beijing, China.

## CONFLICT OF INTEREST

On behalf of all authors, the corresponding author states that there is no conflict of interest.

## REFERENCES

- N. Sumida, T. Fujii, Y. Oguchi, H. Morishita, K. Yoshimura, and F. Sudo: *Kawasaki Steel Tech. Rep.*, 1983, vol. 8, pp. 69–76.
- Y. Luo, C. Liu, Y. Ren, and L. Zhang: *Steel Res. Int.*, 2018, vol. 89, p. 1800048.
- Y. Miki, Y. Shimada, B. G. Thomas, and A. Denisov: *Iron Steelmaker*, 1997, pp. 31–38.
- T. Nakaoka, S. Taniguchi, K. Matsumoto, and S.T. Johansen: *ISIJ Int.*, 2001, vol. 41, pp. 1103–11.
- H. Tozawa, Y. Kato, K. Sorimachi, and T. Nakanishi: *ISIJ Int.*, 1999, vol. 39, pp. 426–34.

**Publisher's Note** Springer Nature remains neutral with regard to jurisdictional claims in published maps and institutional affiliations.

Springer Nature or its licensor (e.g. a society or other partner) holds exclusive rights to this article under a publishing agreement with the author(s) or other rightsholder(s); author self-archiving of the accepted manuscript version of this article is solely governed by the terms of such publishing agreement and applicable law.